Article

Hypereutectic Zn–Al Alloys: Microstructural Development under Unsteady-State Solidification Conditions, Eutectic Coupled Zone and Hardness

Rudimylla Septimio [1,*], Cássio A. P. Silva [2], Thiago A. Costa [3], Amauri Garcia [2] and Noé Cheung [2]

1 Institute of Geosciences and Engineering, Federal University of the South and Southeast of Pará, Unifesspa, Marabá 68050-080, PA, Brazil

2 Department of Manufacturing and Materials Engineering, University of Campinas, Unicamp, Campinas 13083-860, SP, Brazil; cassio.augusto92@gmail.com (C.A.P.S.); amaurig@fem.unicamp.br (A.G.); cheung@fem.unicamp.br (N.C.)

3 Federal Institute of Education, Science and Technology of Pará–IFPA, Belém 66093-020, PA, Brazil; thiago.costa@ifpa.edu.br

* Correspondence: r.septimio@unifesspa.edu.br

Abstract: The present study investigates the effects of Al content and solidification thermal parameters on the microstructural development under transient heat flow conditions for two hypereutectic Zn–Al alloys: Zn-6wt.%Al and Zn-11wt.%Al. The alloys were directionally solidified and had experimental cooling profiles monitored permitting cooling rates and growth rates to be determined along the length of the directionally solidified (DS) castings. The microstructure of the Zn-6wt.%Al alloy is shown to be formed by eutectic colonies, constituted by a eutectic mixture of (Zn) and (Al′) phases in the form of lamellae and the Zn-11wt.% Al alloy by the pro-eutectic (Al′) dendrites and the eutectic mixture in the interdendritic regions. Growth laws are experimentally determined relating eutectic and dendritic spacings to the growth rate and cooling rate. A diagram exhibiting the coupled zone of Zn–Al alloys as a function of cooling rate is proposed, which shows different microstructural morphologies influenced by composition and thermal parameters, that is, growth rate and the temperature gradient, synthesized by the cooling rate ($\dot{T} = G.V$). The microhardness of both Zn-6wt.%Al and Zn-11wt.%Al alloys were shown not to depend on the length scale of the resulting microstructure.

Keywords: Zn–Al alloys; solidification; microstructure; hardness

1. Introduction

Zinc–aluminum-based alloys offer a series of very attractive properties for wide applications in industry, such as to produce automotive parts, electronic/electrical systems and also, water taps and sanitary fittings, household articles, fashion goods, etc. This is because Zn has a lower melting temperature than Al and interesting combinations of mechanical properties, such as tensile strength, elongation, hardness, etc. [1,2]. Other features of these alloys that are widely investigated are wear resistance and corrosion behavior. The excellent tribological properties are based on the behavior of Al and Zn oxides formed; while the Al oxide acts as a load-bearing phase, the Zn oxide acts as a lubricant under near-seizure conditions, being widely used in the manufacture of bearings [3–6]. Moreover, the corrosion behavior of Zn–Al alloys is most broadly exploited due to their greater efficiency as sacrificial coatings for steels [7–9]. Zn–Al alloys also play important roles in the electrical/electronic industries because of their melting point; these alloys are indicated as solder alloys developed for high temperature applications [10–13].

It is well known that different characteristics of Zn–Al alloys result from distinct manufacturing processes and alloying elements content [4]. For example, several works

have shown that the microstructures of these alloys required to achieve certain application properties can be obtained by controlling thermal parameters of solidification, i.e., by modifying the manufacturing process [5,14–17]. Pressure die casting and gravity casting are the most used manufacturing processes in the production of Zn–Al-based alloys [18], which generally result in microstructures composed of eutectic and dendritic phases. Another factor that changes the microstructure is the amount of Al soluble in the Zn-rich matrix and of Al in the eutectic mixture, being 5 wt.% [2]. Therefore, it is expected that the Al content influences the solidification behavior and, consequently, the microstructure evolution [19]. Al- and Zn-rich solid solutions are, respectively, known as (Al) and (Zn) [20,21] or α and η [19,22], which are distributed in a specific manner depending on the Al content and the cooling process during and after solidification. Li et al. [9] studied the effect of Al content on the microstructure of several Zn–Al alloys coatings and found that the Zn-0.6wt.%Al alloy consists of equiaxed η-Zn grains surrounded by narrow grain boundaries, while the Zn-1.5wt.%Al alloy is formed by η-Zn grains, Zn–Al dendritic eutectoid structure and lamellar Zn–Al eutectoid structure. They observed that the increase in the alloy Al content up to 3wt.% and 6wt.%Al changes the microstructure considerably. The Zn-3wt.%Al alloy presented shrunken η-Zn grains and a sharp increase in the amount of eutectoid structure, while in the Zn-6wt.%Al alloy the η-Zn grains disappeared completely, resulting only in presence of dendritic Zn–Al eutectoid structure and lamellar Zn–Al eutectoid structure. Bansod et al. [23] also studied Zn–Al alloys having quite different Al contents (1; 2.5; 4.5; 6; 6.5; 8.5; 11.5; 25; 55 wt.% Al) and observed that the increase in the alloy Al content intensifies the formation of dendrites. El-khair et al. [22] observed that the microstructure of a Zn-8wt.%Al alloy has coarse η-Zn rich dendrites and $\alpha + \eta$ eutectoid colonies, while the Zn-12wt.%Al alloy has a more refined η-Zn rich phase and the presence of eutectoid colonies in greater quantity as compared with the Zn-8wt.%Al alloy. Besides, the Zn-27wt.%Al alloy microstructure consists of α-Al rich dendrites surrounded by $\alpha + \eta$ eutectoid colonies. On the other hand, studies analyzing the influence of solidification cooling conditions are rare in the literature.

Although several studies on Zn–Al alloys can be found in the literature, agreement on a specific eutectic composition was not found, with several works that use the range from 4 to 6wt.% Al [2,6,7,24,25]. However, Kurz [26] affirms that the microstructure can vary not only with the alloy composition, but depends also on the solidification thermal parameters, i.e., a desired microstructure can be obtained within a certain range of composition and thermal parameters. So, a solidification microstructural selection map (SMSM) can be set, considering the transition between a completely eutectic structure and primary dendrites or cells surrounded by the eutectic structure. In this diagram, the coupled zone defines the limits of the thermal parameters and compositions for fully eutectic microstructures. Silva et al. [27] studied the microstructure evolution of some Al–Co alloys and proposed an SMSM plot relating growth and cooling rates to the Co composition, thus permitting a coupled growth zone to be determined. Kakitani et al. [28] studied a range of alloys compositions of the Sn–Cu and Sn–Bi systems and they also proposed SMSM's relating growth rate to thermal gradient in or around the eutectic composition comprising the influences of both solidification thermal parameters on the microstructure growth. Although several compositions of Zn–Al alloys have already been studied, to the best of the present authors' knowledge, extensive information leading to thermal parameters correlations with microstructures that could allow the development of the coupled zone, comprising a wide range of alloy compositions, cannot be found in the literature. Moreover, so far, no SMSM for the Zn–Al alloy system has been proposed. In this sense, such map could provide a better understanding on the microstructural growth of commercial Zn–Al-based alloys solidified under industrial conditions, i.e., non-stationary heat flow conditions.

Recent studies show that Zn–Al alloys have promising applications as metallic coatings, mainly with additions of Mg [29–31]. Rai et al. [29] show that the improvement in the corrosion resistance of steel coated with a Zn–Al–Mg alloy is due to preferential

dissolution of $MgZn_2$ present in the interdendritic regions of Zn-rich phases, promoting better sacrificial protection. However, the available literature does not address the influence of the manufacturing parameters on the resulting microstructure, which are related in the present work to the solidification cooling rate. According to Prosek et al. [32], the mass losses due to corrosion for Zn-5wt.%Al and Zn-3wt.%Al-2wt.%Mg alloys, used as steel coatings, vary up to two times as a function of their microstructures. Considering that metallic coatings deal with rapid cooling, this investigation would contribute to the understanding of microstructures solidified out of equilibrium conditions since Zn–Al binary alloys are the base of these alloys for coating purposes.

The present study aims to investigate the effects of Al content and solidification thermal parameters on the microstructural development under transient heat flow conditions for two hypereutectic Zn–Al compositions: Zn-6wt.%Al and Zn-11wt.%Al. A water-cooled solidification device is used to provide a wide range of cooling rates and, consequently, a variety of resulting microstructures in a single experiment. The effect of the Al content on the microhardness is also analyzed. Besides, this investigation seeks to contribute to a better understanding of the coupled zone of the Zn–Al system, providing a SMSM diagram involving data from the present study and results from the literature for Zn–Al alloys in a range of Al contents from 0.5 to 11 wt.%.

2. Materials and Methods

The studied Zn–Al alloys were prepared from weighed quantities of commercially pure Zn and Al, and their chemical composition are shown in Table 1. The alloys were melted in a SiC crucible inside a muffle furnace (Brasimet, Jundiaí, Brazil) and poured into the mold of a directional solidification device (Figure 1). The mold is made of stainless-steel and has an internal diameter of 60 mm, height of 110 mm and wall thickness of 3 mm, which is internally coated with alumina to avoid contact between liquid metal and mold. The bottom part of the mold was closed with a thin (3 mm thick) polished carbon steel sheet, which was quenched by water at room temperature. Such set up promotes the directional transient solidification by extracting heat through a water-cooled mold bottom, thus permitting a wide range of cooling rates to be operative along the length of the casting. To measure the temperatures along the casting, a bank of fine type K thermocouples was positioned at different positions along the casting length, from the heat-extracting surface at the bottom of the casting (as shown in Figure 1). The position of each thermocouple was measured at the post-mortem casting longitudinal sections containing the thermocouple tip. All thermocouples were connected by coaxial cables to a data logger (Lynx, São Paulo, Brazil) of 12 bits using a frequency of 5 Hz to record the thermal history in a computer. Figure 2 shows the partial view of the Zn–Al phase diagram, where the Zn–6wt.%Al alloy is indicated by a black dotted vertical line and the Zn–11wt.%Al alloy by a red dotted vertical line. The phase diagram was used to determine the liquidus temperature (T_L). For each alloy, the solidification onset was established when the temperature stabilized at 10% above T_L.

Table 1. Composition of the metals used to prepare the Zn–Al alloys.

wt.%	Al	Zn	Fe	Si	Mg	Cu	Pb
Al	Balance	0.01	0.03	0.03	0.01	0.01	-
Zn	-	Balance	0.015	0.003	-	-	0.012

From the experimental cooling profiles obtained from the thermocouples, it was possible to determine the displacement of both liquidus and eutectic isotherms along the length of the directionally solidified alloys castings through correlations between the thermocouple positions (P), with respect to the cooled casting base and related times (t) of each isotherm passing by each thermocouple. Thus, the power function ($P = a.t^b$, being a and b constants) can adequately represent the correlation between P and t to fit the experimental data. A time-derivative of these functions results in the liquidus and eutectic

growth rates (V_L, V_E), and the time-derivative (dT/dt) permits the liquidus and eutectic cooling rates ($\dot{T}_L$, $\dot{T}_E$) to be determined.
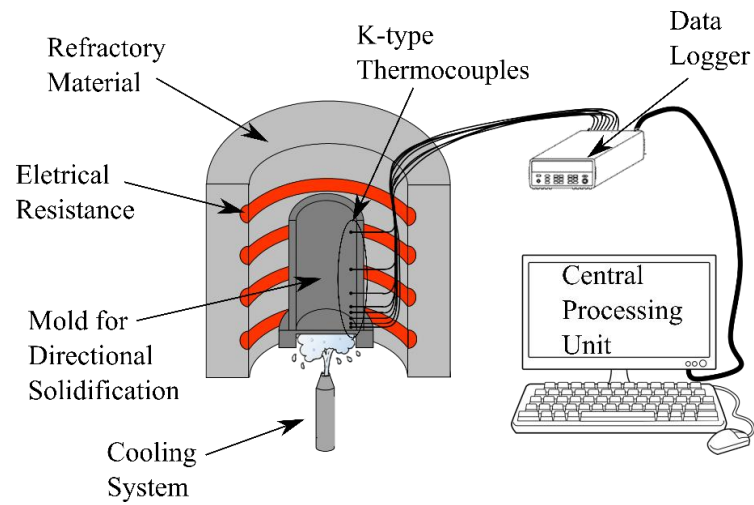

Figure 1. Schematics of the vertical upward directional solidification device.
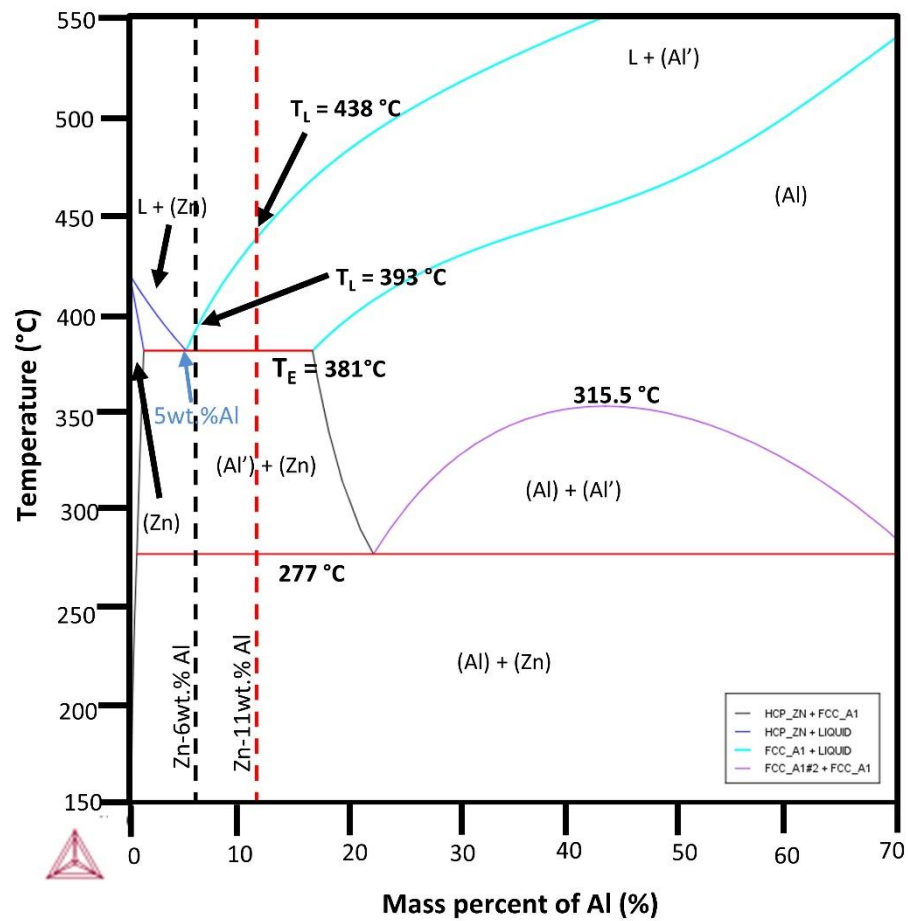

Figure 2. Partial phase diagram of the Zn–Al system calculated by the ThermoCalc software (TCS Solder Alloy Solutions version 3 Database [33]).

Poulton's reagent (HF, HCl, HNO$_3$ and water) for 10 s was used in order to reveal the macrostructure of the DS castings. Moreover, samples were extracted from longitudinal and transversal sections along the length of each casting (Figure 3), with a view to characterizing the microstructure evolution from the cooled bottom towards the top of the castings. As can be seen in Figure 3, the morphologies of microstructures of Zn6wt.%Al and Zn-11wt.%Al alloys are characterized by eutectic colonies and dendritic arrangement, respectively. The samples were grounded with sandpapers until 1200 grit, and then finely polished with diamond paste (6 and 1 µm). No etching was necessary to reveal the microstructure of the samples.
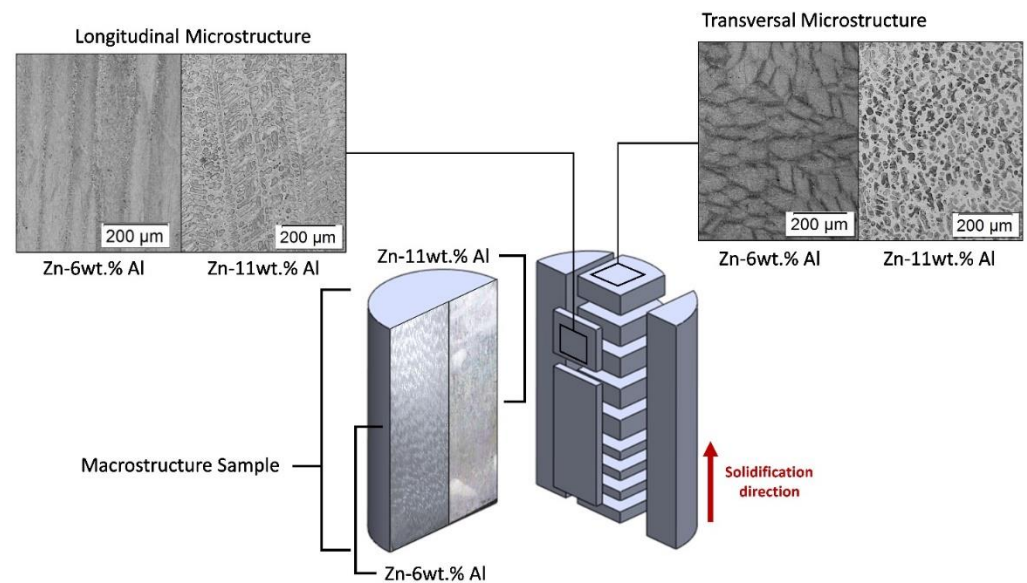

Figure 3. Schematic representation of samples extracted along the length of the castings for further microstructural characterization.

An X-ray fluorescence spectrometer (XFR), (model Rigaku RIX, 3100, Tokyo, Japan) was used to estimate local average composition through an area of 100 mm^2 probe at each transversal sample for segregation analysis. X-Ray diffractometry (XRD) was performed in range of $20° > 2\theta > 90°$ to determine phases at different positions along the length of the DS castings; for this a Cu-kα target with Ni filter with voltage of 45 kV and current of 40 mA was used in the diffractometer (X'Pert Pro MRD XL, Malvern Panalytical, Cambridge, UK). The examination of the microstructure was carried out using an optical Olympus Inverted Metallurgical Microscope (model 41GX, Olympus, Tokyo, Japan) and the Back Scattered Electron imaging (BSE) of the Scanning Electron Microscope (ZEISS-EVO-MA15, Zeiss Microscopy, Oberkochen, Germany), equipped with Oxford X-Max model Energy Dispersive Spectrometer (EDS) (Zeiss Microscopy, Oberkochen, Germany), was used to complement the microstructural characterization. Correlations between the microstructure and the solidification thermal parameters were established considering the representative isotherms (liquidus (T$_L$) and eutectic (T$_E$)) of each alloy, indicated in the Zn–Al phase diagram (Figure 2). The microstructural features considered in this investigation were eutectic colony spacing (λ_{EC}), eutectic lamellae spacing (λ_L), primary dendritic arm spacing (λ_1) and secondary dendritic arm spacing (λ_2). The measurement of the eutectic colony spacing and primary dendritic arm spacing were obtained by using the triangle method [34] and the eutectic lamellar spacing by the average distance considering five lamellae [34,35]. The secondary dendritic arm spacings were obtained using the intercept method [36].

Vickers microhardness tests were performed on the cross sections surfaces of the samples using a Shimadzu HMV-2 model hardness measuring (Shimadzu, Kyoto, Japan). The parameters for hardness measurement were chosen based on some Zn-based alloys investigations [37–40]. The test load of 0.5 kgf and a dwell time of 10 s were the best

parameters to analyze hardness, in which the indentation was not too big, making the measurement possible, and not too small, to avoid measurement uncertainties. A total of 25 indentations were performed for each sample.

3. Results and Discussion

3.1. Solidification Thermal Parameters and Chemical Analysis

The cooling profiles during the solidification experiments, obtained by six thermocouples positioned inside the DS castings, are shown in Figure 4. The dotted and straight lines in each graph indicates the liquidus (T_L) and eutectic (T_E) temperatures, respectively. Analyzing the experimental cooling profile, the solidification started at higher temperatures for the higher Al content alloy, i.e., the increase in Al content in the alloy promotes the rise of T_L from 392 °C (Zn-6wt.%Al) to 438 °C (Zn-11wt.%Al). For the thermocouples closer to the cooled bottom of the mold, the cooling curves are related to higher heat extraction rates and, consequently, the sharpest temperature decrease is realized for early solidification times. On the other hand, for the thermocouple positioned far from the cooled bottom of the casting, the heat extraction rates decrease progressively due to the increasing thermal resistance associated with the increase in the solidified layer from the cooled base of the casting. Figure 5 shows the experimental profile of liquidus and eutectic isotherms displacements. It can be observed that the isotherms of the Zn-11wt.%Al casting are faster than those of the Zn-6wt.%Al casting.
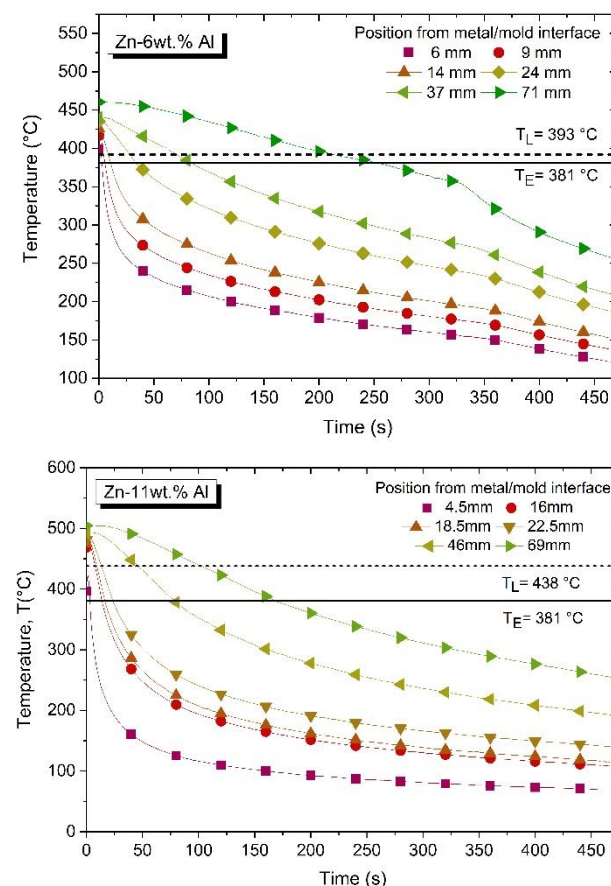

Figure 4. Cooling profiles along the length of the DS Zn-6wt.%Al and Zn-11wt.%Al alloys castings.

The cooling rate profiles related to the liquidus, and the eutectic isotherms are shown in Figure 6. A power function of the form $\dot{T} = cP^{-d}$, being c and d constants, is fitted to the experimental points along the length of each alloy casting. The cooling rate profiles of both Zn-6wt.%Al and Zn-11wt.%Al alloys castings show that at positions close to the cooled bottom of the castings the solidification process occurs at high cooling rates. Besides,

comparing both alloys, it can be observed that the alloy with lower Al content presents a lower profile of cooling rates along the length of the casting. This may be associated with both a lower metal/mold wettability in the early solidification stages of the casting [41] and thermal properties of the alloy, such as a lower thermal conductivity of the alloy having lower aluminum content, since Al has a thermal conductivity higher than that of Zn [42,43].
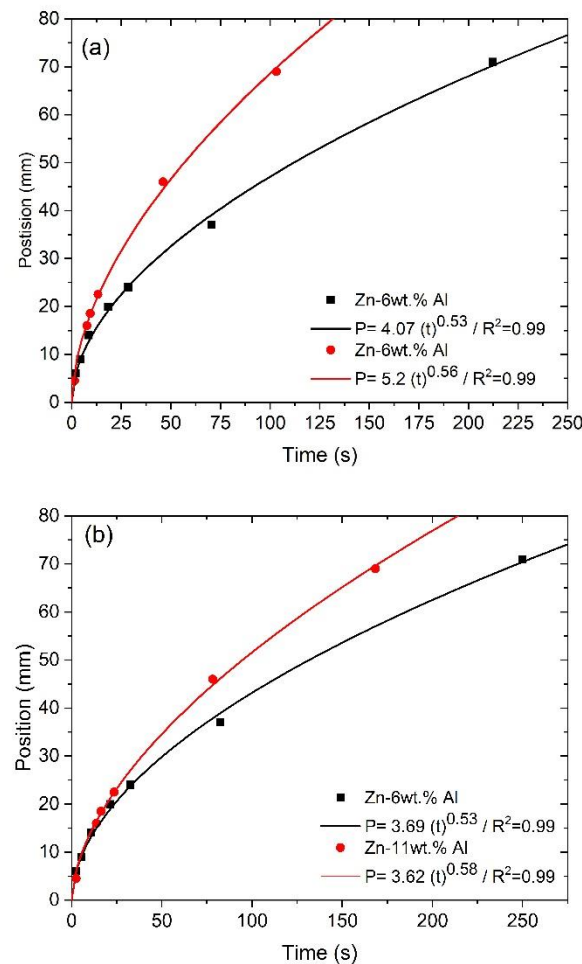

Figure 5. Experimental displacement of liquidus and eutectic isotherms along the length of the DS alloys castings, where: P (mm) is the thermocouple position from the cooled bottom of the casting and t (s) is time: (**a**) liquidus isotherm and (**b**) eutectic isotherm. R^2 is the coefficient of determination.

The growth rate, i.e., the velocity of displacement of each isotherm, as a function of the thermocouple positions is depicted in Figure 7. For the liquidus isotherm, it can be noted that the Zn-11wt.%Al alloy presents a higher growth rate profile than that of the Zn-6wt.%Al alloy, mainly at positions closer to the cooled bottom of the casting. The increase in the alloy Al content, as shown in the Zn–Al phase diagram (Figure 2), influences the solidification range. Since the Zn-11wt.%Al presents a larger solidification range, consequently, it releases a larger amount of latent heat before the eutectic transformation, which changes the solidification kinetics. Concerning the displacement of the eutectic isotherm, for both alloys the results are quite the same, since the eutectic latent heat is all released in a single temperature (T_E). In contrast, different profiles of cooling rates $\dot{T}_E$ were realized in Figure 6b, which can be explained due to different thermal gradient profiles ahead of the eutectic isotherm (G_E), given by the relation $G_E = \dot{T}_E/V_E$ [44].
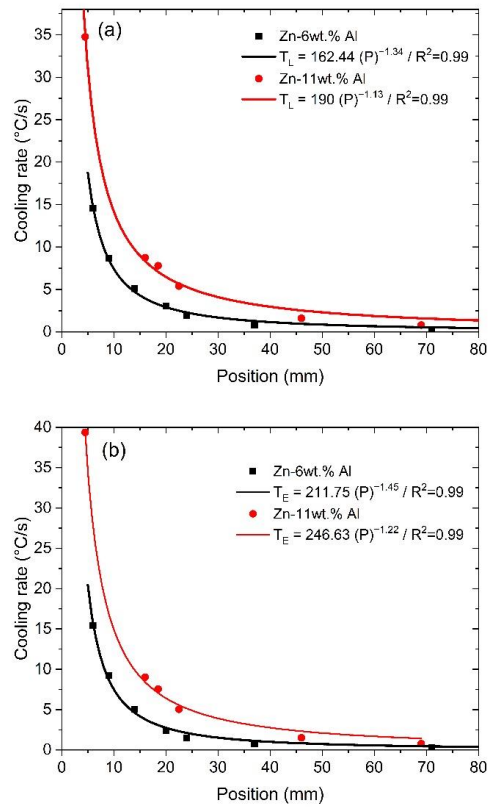
Figure 6. Cooling rates as a function of P for the Zn–6wt.% Al and Zn–11wt.% Al alloys castings: (**a**) liquidus isotherm ($\dot{T}_L$), and (**b**) eutectic isotherm ($\dot{T}_E$).
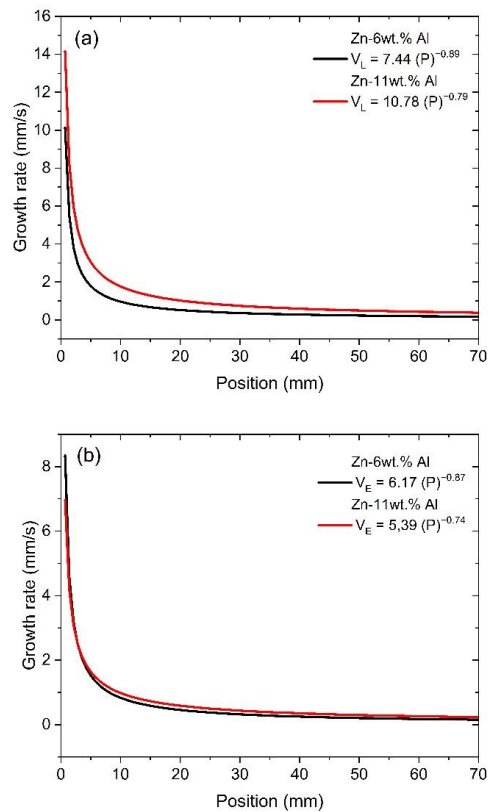

Figure 7. Growth rates as function of P for the Zn–6wt.% Al and Zn–11wt.% Al alloys castings: (**a**) liquidus isotherm (V_L), and (**b**) eutectic isotherm (V_E).

Figure 8 shows the solute profiles along the length of the DS castings, determined by X-ray fluorescence. For both Zn–Al alloys, the composition of Al remained approximately constant and close to the nominal Al concentration of each alloy, which does not configure the occurrence of macrosegregation.
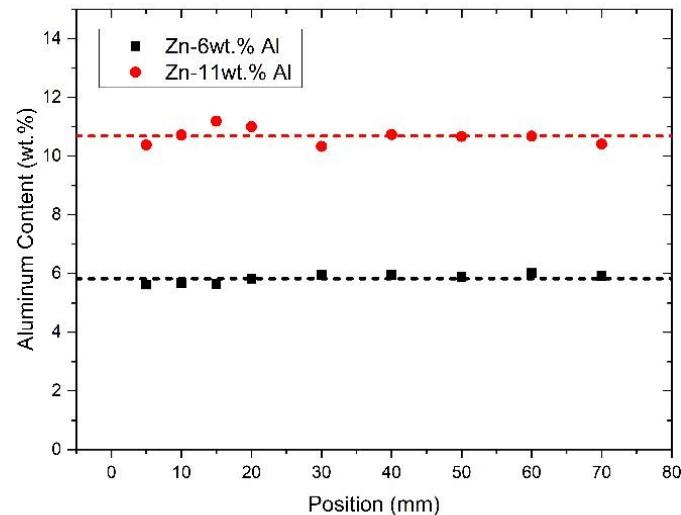

Figure 8. Al concentration profiles along the length of the DS Zn–Al castings.

3.2. Microstructural Characterization: Optical Microscopy (OM), Scanning Electron Microscopy (SEM) and X-ray Diffraction (XRD)

According to the binary phase diagram (Figure 2), the studied alloys are hypereutectic alloys, so their microstructural morphology is expected to consist of Al-rich dendrites and Zn/Al eutectic mixture [23]. Figure 9 shows the evolution of solid phases fractions versus temperature for the Zn-6wt.%Al and Zn-11wt.%Al alloys in equilibrium, according to the ThermoCalc software (database SSOL6-2019a, Thermocalc, Basel, Switzerland). It is possible to conclude that, under equilibrium conditions, the Zn (HCP_ZN) and Al′ (FCC_L12) phases are present in the microstructures of the investigated alloys according to the following proportions: Zn-6wt.%Al→6 wt.% Al′ (FCC_L12) + 94 wt.% Zn (HCP_ZN) and; Zn-11wt.%Al→11 wt.% Al′ (FCC_L12) + 89 wt.% Zn (HCP_ZN). The temperature that characterizes the beginning of the formation of the first solid particles (Al-rich dendrites-(Al′) phase), that is, the liquidus temperature, is 393 °C and 438 °C, for Zn-6wt.%Al and Zn-11wt.%Al alloys, respectively. Analyzing the slope of the liquid phase curve (dashed line) it is observed that the solidification interval is shorter for the Zn-6wt.%Al alloy. The eutectic and eutectoid reactions are expected to occur at 381 °C and 277 °C, respectively, for both alloys. Solid phase transformation between this temperature range (381–277 °C) occurs in which the (Zn) phase (HCP_ZN) grows from the (Al′) phase (FCC_L12). At the eutectoid temperature (277 °C), another solid transformation occurs (Al′)→(Al) + (Zn).

Figures 10 and 11 show the typical microstructures of the DS Zn-6wt.%Al and Zn-11wt.%Al alloys castings, respectively. The microstructures were characterized from both transverse and longitudinal sections of the samples using optical microscopy (OM) and scanning electron microscopy (SEM) techniques. For the Zn-6wt.%Al alloy, as can be observed in Figure 10a,b, the eutectic colonies are constituted by a eutectic mixture of (Zn) and (Al′) phases in the form of lamellae. Moreover, since (Al′) is a metastable phase, it undergoes a eutectoid transformation at 277 °C [(Al′)→(Al)→(Zn)], as previously mentioned. Hence, as can be seen in Figure 10a at higher magnification (10,000×), the resulting microstructure is composed also by lamellae (Al dark phase + Zn gray phase) neatly distributed over a Zn-rich matrix (the gray phase). For hypereutectic Zn–Al alloys close to the eutectic composition, the Al-rich dendrites, composed by primary metastable phase (Al′), are expected to be formed in a narrow range of temperatures, between the liquidus temperature (T_L) and the eutectic temperature (T_E), which would precipitate from the global liquid

(L). However, in eutectic alloy systems, a competition between the eutectic structure and the primary phase determines the resulting microstructure for alloy compositions near the eutectic invariant point. A near eutectic alloy may present a fully eutectic microstructure if the growing phase takes precedence over the primary phase. Otherwise, the resulting microstructure may be characterized by the dominant primary phase [45]. In this case, the primary phase has been suppressed, i.e., the high cooling rates imposed by the transient solidification may induce the lamellar eutectic growth before the dendrites formation. The literature states that during the solidification process, high cooling rates may induce the precipitation of unexpected phases for a given composition or may even suppress the formation of the phases predicted for equilibrium conditions [46–48]. Solidification of a eutectic phase encompasses a diffusive coupling process of high efficiency, which can be faster than the isolated growth of a single phase, i.e., primary dendrites, even for alloys of pro-eutectic composition [49]. At high cooling rates, dendritic growth may be contained by the faster growth of the eutectic, and, consequently, purely eutectic microstructures can be obtained for near eutectic compositions. Porot et al. [25] demonstrated the growth of eutectic colonies for the hypereutectic Zn-5.5wt.%Al alloy solidified under high cooling rates. The same microstructure change was observed to occur in different hypereutectic alloys: Al-Al$_2$Cu [50]; Al–Fe [26]; Al–Si [51]; Co–Sn [52]. A solidification microstructure selection map, encompassing a range of growth and cooling rates, for the Zn–Al alloys will be further presented in a specific section.

The typical microstructure of the Zn–11wt.% Al alloy is shown in Figure 11. The microstructure is characterized by the presence of pro-eutectic (Al′) dendrites and interdendritic regions composed by the eutectic mixture [(Al′) + (Zn)]. It is worth mentioning that both the dendritic pro-eutectic (Al′) phase and the (Al′) lamellae phase of the eutectic mixture are formed by the product of the eutectoid transformation [(Al′)→(Al) + (Zn)], with Al being the darker region, and Zn, the lighter region. The microstructural analysis performed at the longitudinal section of the DS casting (Figure 11b) revealed that the primary phase developed in the form of columnar dendrites. A previous study performed with the hypereutectic Zn-8wt.%Al and Zn-8wt.%Al-Xwt.%Bi (X = 1.5, 2.3, and 3.0) alloys, solidified under unsteady-state heat flow conditions, has shown that the primary phase developed in the form of predominantly equiaxed dendrites for both binary and ternary alloys [20]. The change in the dendrite structure may be related to the increase in the alloy Al content.
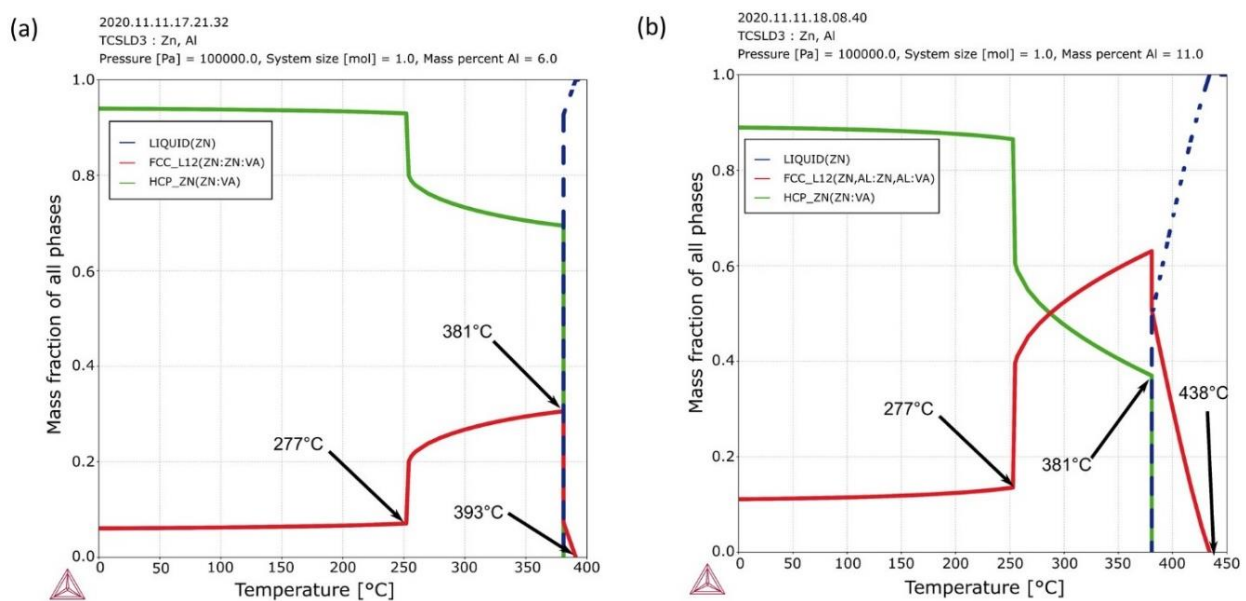

Figure 9. Equilibrium phase fractions versus temperature according to the ThermoCalc software, TCSLD3 Data base, for: (**a**) Zn-6wt.% Al and (**b**) Zn-11wt.% Al alloys [33].
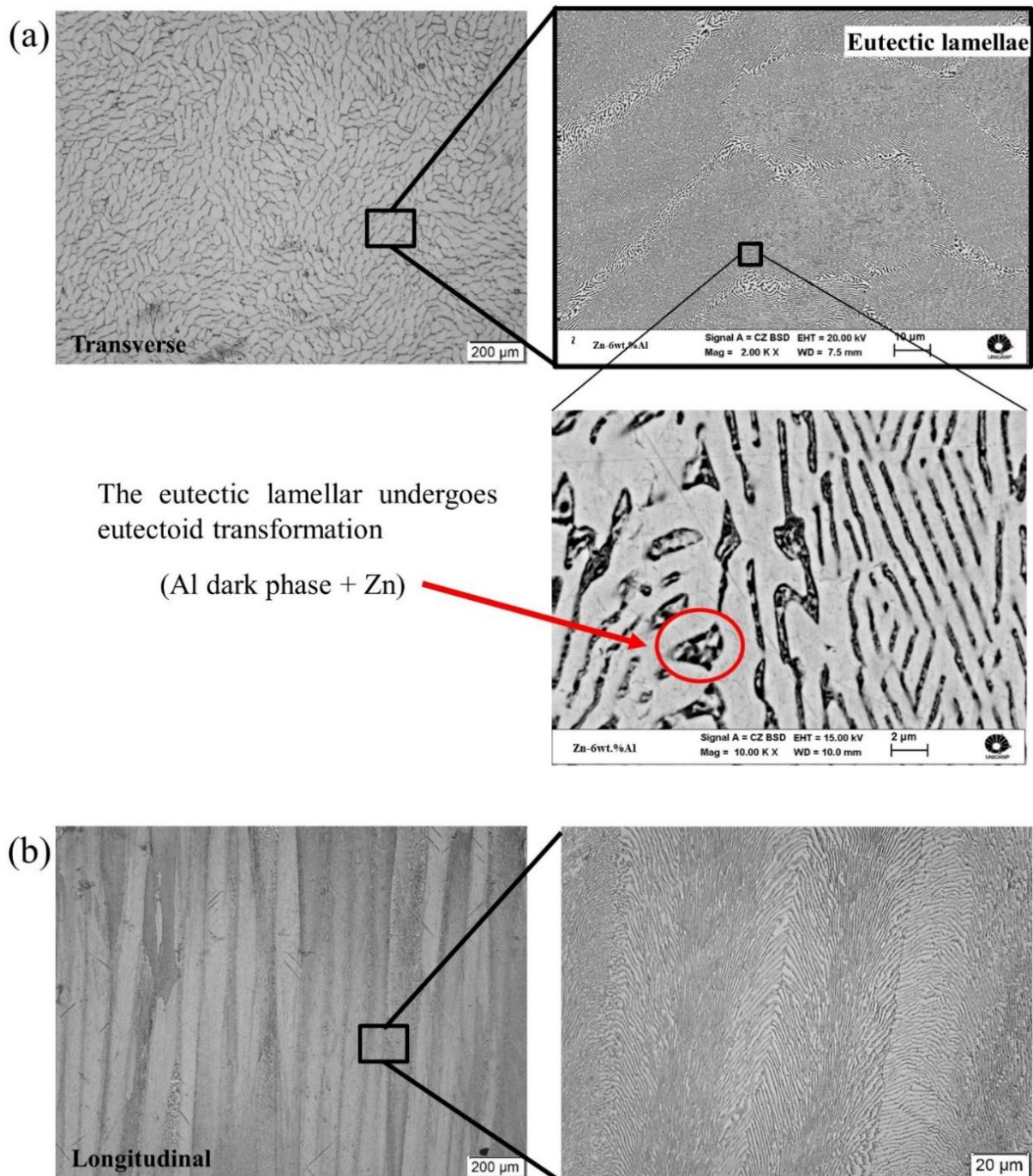
Figure 10. Typical microstructure of the Zn–6wt.% Al alloy highlighting a eutectic lamella in (**a**) transverse and (**b**) longitudinal sections of the DS casting. The sample was extracted at 10 mm from the cooled bottom of the casting.

To confirm the aforementioned phases, XRD analyses were carried out on two samples extracted from each DS Zn–Al alloy casting, subjected to different solidification cooling rates. From these results in Figure 12, pattern indexing established a Zn phase and an Al phase, confirming that the eutectoid transformation has occurred from the (Al′) phase into (Al) and (Zn).
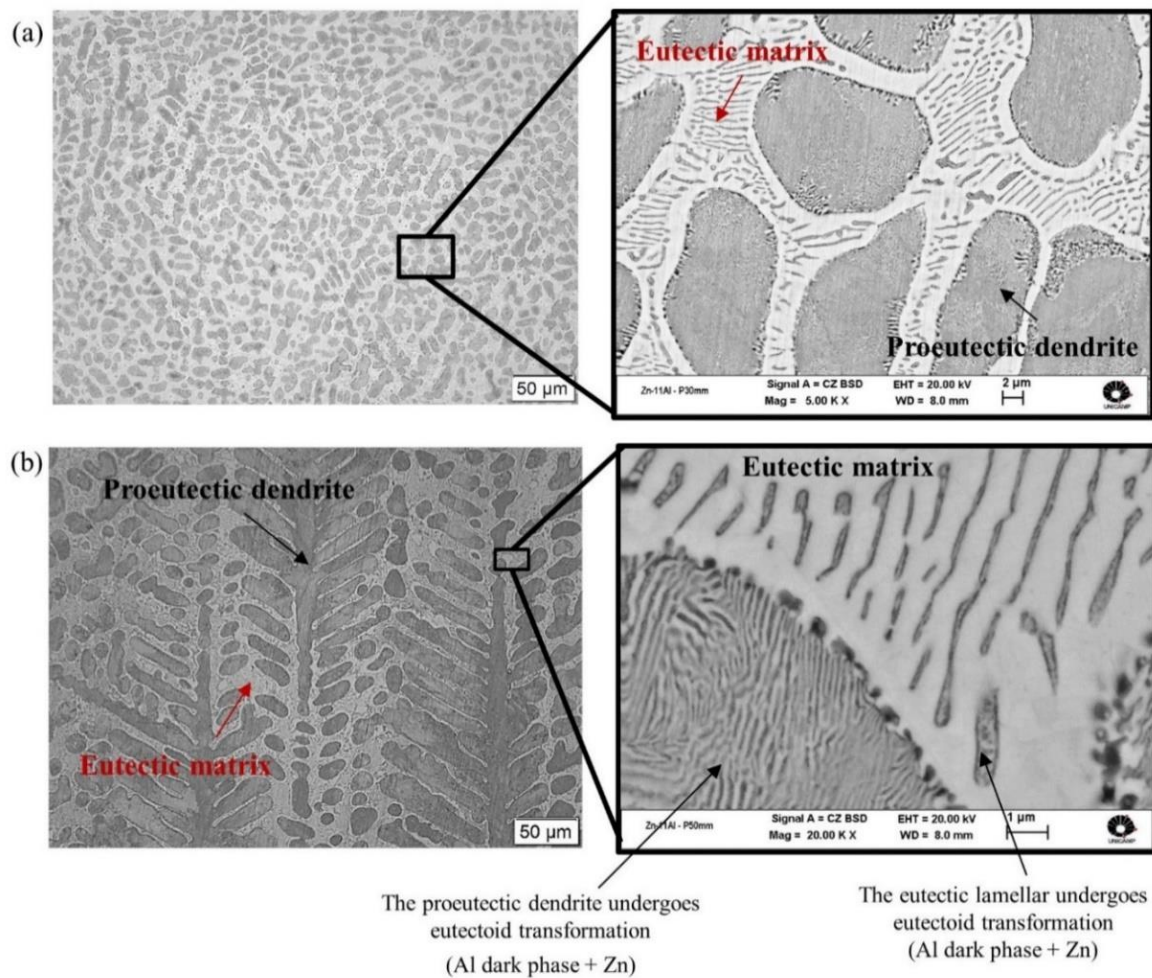
Figure 11. Typical microstructure of the Zn–11wt.% Al alloy highlighting a eutectic lamella in a (**a**) transverse and (**b**) longitudinal sections of the DS casting. The samples were extracted at 30 mm and 50 mm from the cooled bottom of the casting, respectively.
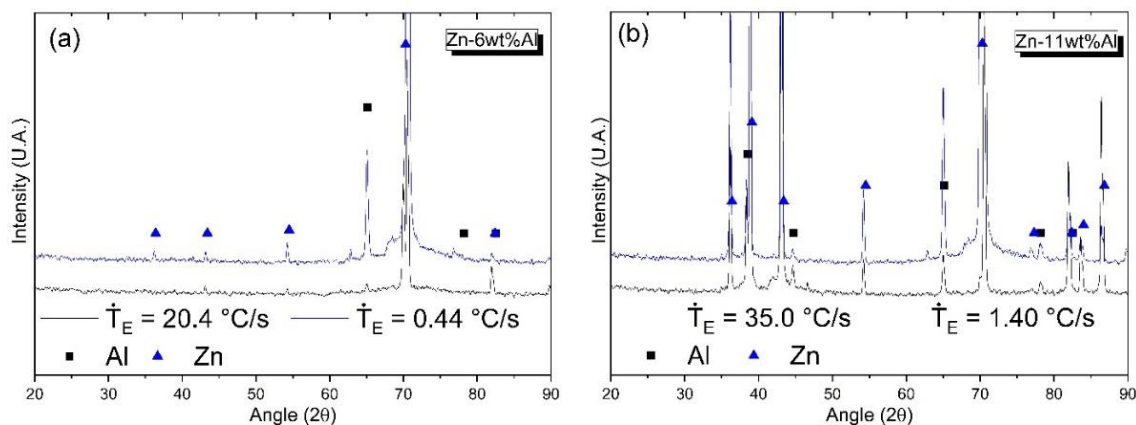

Figure 12. X-ray diffractograms of samples from the DS casting subjected to different cooling rates (**a**) Zn-6wt.%Al and (**b**) Zn-11wt.%Al.

For better visualization of the thermal parameters effect on the microstructure, optical micrographs of transverse and longitudinal sections were chosen at three different positions along the length of the DS castings to illustrate the evolution of the microstructures for high, medium and low solidification cooling rates (Figures 13 and 14). The values of cooling

rates, growth rates and secondary dendritic arm spacings are also shown in each figure. It can be clearly seen that the microstructure is more refined at higher growth and cooling rates and becomes coarser as the rate decreases.
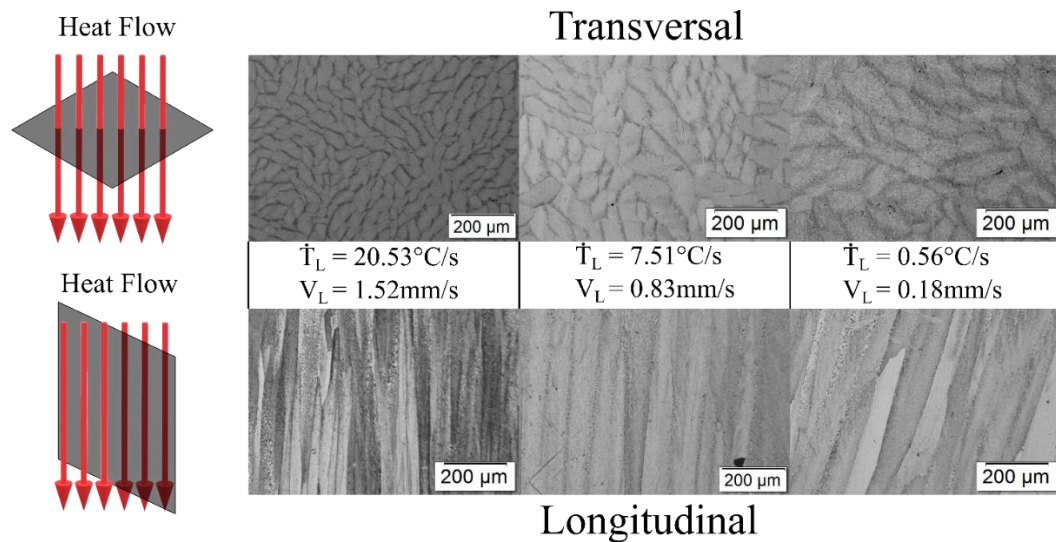

Figure 13. Typical microstructures along the length of the DS Zn-6 wt.% Al alloy casting. [$\dot{T}_L$ = cooling rate of liquidus isotherm, and V_L = growth rate of liquidus isotherm].
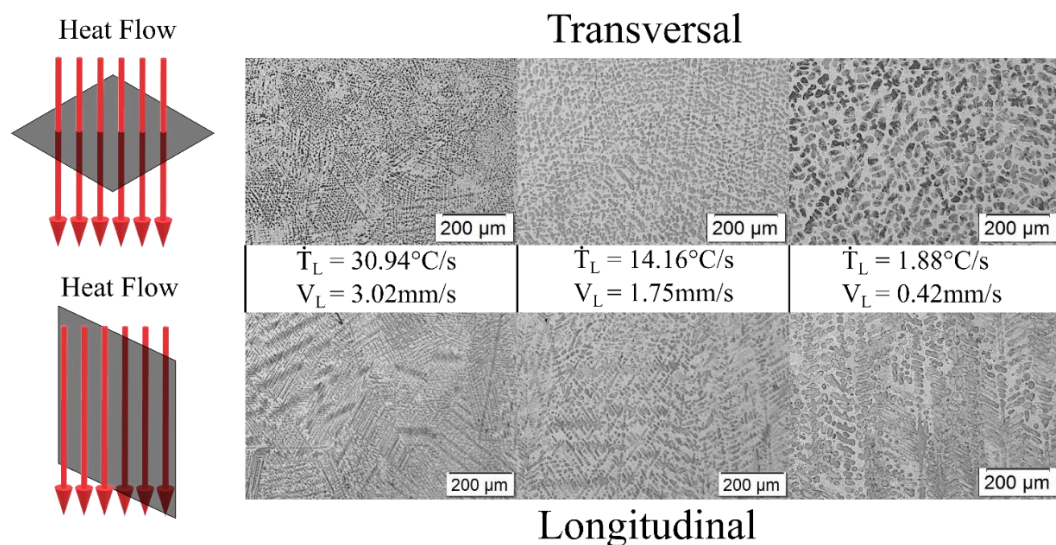

Figure 14. Typical microstructures along the length of the DS Zn-11wt.% Al alloy casting. [$\dot{T}_L$ = cooling rate of liquidus isotherm, and V_L = growth rate of liquidus isotherm].

3.3. Microstructural Growth and Correlation with Solidification Thermal Parameters

Correlations between the microstructure and the thermal parameters were established considering the representative isotherms (liquidus and eutectic). The microstructure parameters considered in this investigation were: eutectic colony spacing (λ_{EC}), eutectic lamellae spacing (λ_L), primary dendritic arm spacing (λ_1), and secondary dendritic arm spacing (λ_2). The data were plotted, where each point represents the average experimental microstructural spacing and the maximum and minimum bars. These bars are not visible for the (λ_{EC}) plot due to the axis scale. Power functions for the growth laws were used to adjust the experimental points and experimental equations are proposed to describe λ vs $\dot{T}$ and λ vs V evolutions.

Figure 15 shows the influence of the thermal parameters on the eutectic colony spacing (λ_{EC}) for the Zn-6wt.%Al alloy, and on the eutectic lamellae spacing (λ_L) for the Zn-11wt.%Al alloy. The adjusted scaling laws relating λ_{EC} to V_E and $\dot{T}_E$ are power functions typified by $-1/2$ and $-1/4$ exponents, respectively. These exponents follow the classical relationship for the lamellar eutectic growth proposed by Jackson and Hunt, where $\lambda^2 V = $ constant [53]. Since the cooling rate is given by a constant multiplied by V^2 [54] and replacing it into the aforementioned Jackson–Hunt expression, the resulting expression for λ can be expressed as a function of $\dot{T}^{-1/4}$. Such exponents values have been used to describe the growth of eutectic colonies for Al-6.3wt.%Ni [55] and Bi-2.5wt.%Ag alloys [56]. The experimental values of λ_L of the hypereutectic Zn-8wt.%Al alloy that solidified under transient conditions were also shown to fit the classical eutectic growth law [20] with the expression $\lambda_L = 0.35 V_E^{-1/2}$ and $\lambda_L = 0.75 \dot{T}_E^{-1/4}$.
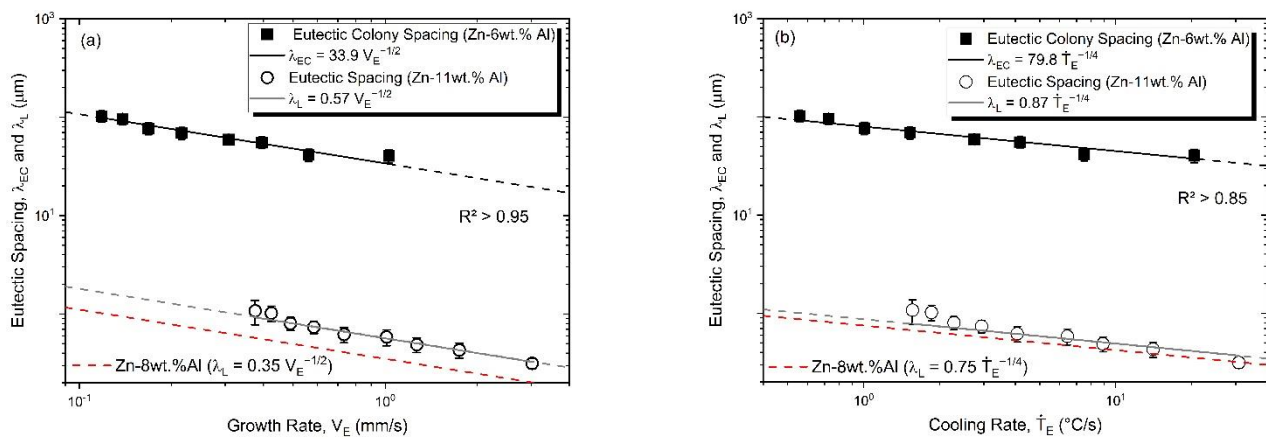

Figure 15. Eutectic cell and eutectic lamellae spacing as a function of solidification thermal parameters of the Zn–Al alloys: (**a**) growth rate and (**b**) cooling rate.

The increase in either cooling rate or growth rate induces a decrease in the microstructural spacing [57,58]. The primary dendritic arm spacing (λ_1) as a function of solidification thermal parameters for the DS Zn-11wt.%Al alloy casting is depicted in Figure 16. Power function growth relationships are shown to describe the experimental evolution of the primary dendritic spacing (λ_1) with growth rate (V_L) and cooling rate ($\dot{T}_L$) with -1.1 and -0.55 exponents, respectively. Such power functions are recognized as the most appropriate based on a number of experimental evidences in recent studies, considering the growth of primary dendrite arm spacings under transient solidification conditions [16,59–61].
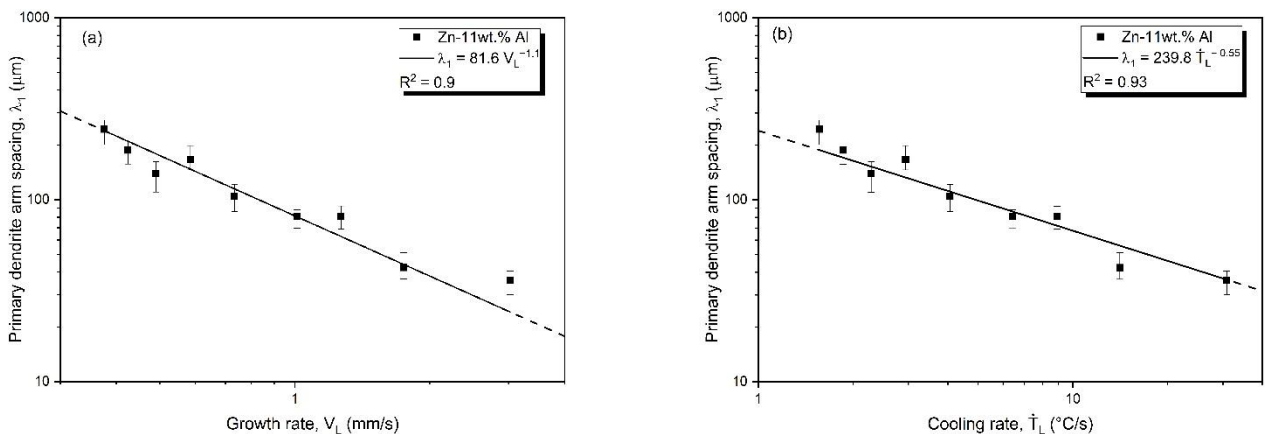

Figure 16. Primary dendritic arm spacing as a function of solidification thermal parameters of the Zn-11wt.%Al alloy: (**a**) growth rate and (**b**) cooling rate.

The secondary dendritic arm spacing (λ_2) as a function of thermal parameters is displayed in Figure 17. The data are compared with an experimental growth law of the hypereutectic Zn-8wt.%Al alloy [20], also solidified under transient conditions. It can be observed that high cooling and growth rates are related to decreasing λ_2. The power function growth relationships describing the experimental evolution of secondary dendritic arm spacing (λ_2) with growth rate (V_L) and cooling rate ($\dot{T}_L$) are characterized by $-2/3$ and $-1/3$ exponents, respectively, for Zn-11wt%Al and Zn-8wt.%Al alloys. The power functions that describe the λ_2 growth as a function of V_L have also been used for the Zn-3wt.%Al and Zn-4wt.%Al alloys, solidified under transient conditions [15]. It can be seen that there is an increase in the secondary dendritic arm spacing with the increase in the Al alloy content. Bansod et al. [23] investigated the effect of addition of Al in Zn by microstructural examination of Zn-Xwt.% Al alloys (X = 1; 2.5; 4.5; 6; 6.5; 8.5; 11.5; 25; 55). The authors noted that the increase in Al content of the alloy results in the increase in the (Al') phase fraction and coarser dendrites. For the Zn-25wt.%Al and Zn-55wt.%Al alloys, the microstructure was shown to be formed by dendrites with a small quantity of eutectic mixture.
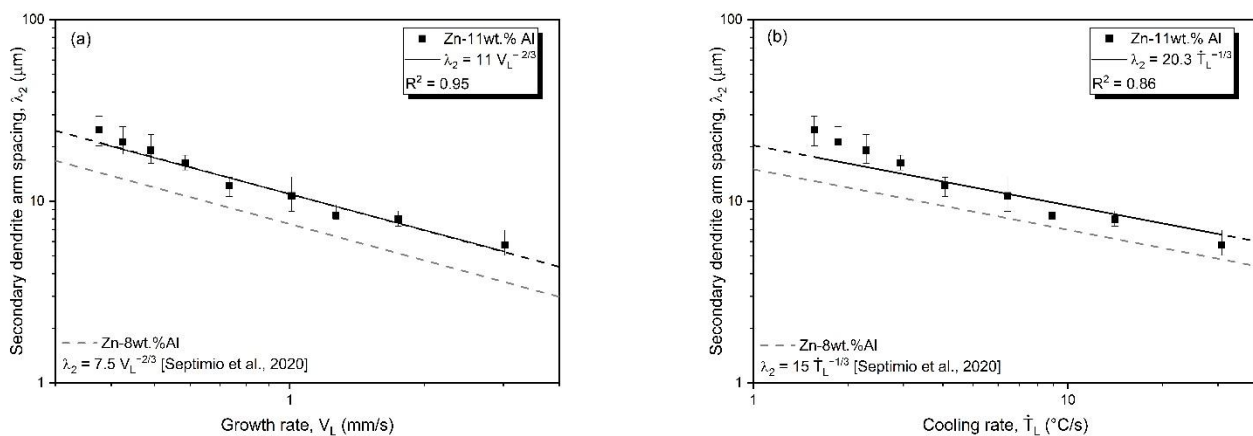

Figure 17. Secondary dendritic arm spacing as a function of solidification thermal parameters for the Zn-11wt.%Al alloy: (**a**) growth rate and (**b**) cooling rate.

3.4. Coupled Zone

A diagram exhibiting the coupled zone of Zn–Al alloys as a function of the cooling rate ($\dot{T}$), obtained in the present study, is depicted in Figure 18, which shows different microstructural morphologies influenced by composition and thermal parameters, that is, the growth rate and the temperature gradient, both synthesized by the cooling rate ($\dot{T} = G.V$). Data from previous studies [20,52–56] were also added to the map in order to complement the analysis. Regarding hypereutectic alloys, Tunca and Smith [62] examined directionally solidified Zn–Al alloys with 6.5 wt.%, 8 wt.% and 11 wt.% of Al, and they found dendrites composed by two phases along a cooling rate range from of 7.47 to 0.07 °C/s because of the eutectoid transformation that occurs in Zn–Al hypereutectic alloys. According to the results of the present study, the 6wt.%Al seems to be the limit in Al concentration that allows obtaining eutectic structure in Zn–Al alloys. For hypoeutectic compositions, Ares et al. [63] investigated the microstructure of Zn alloys with 1, 2, 3 and 4 wt.% Al, and they observed that the microstructure of these alloys is composed of Zn-rich dendrites and eutectic mixture along a solidification cooling rate range from of 1.2 to 2.3 °C/s, as expected. Nonetheless, Pastene et al. [64] studied the behavior of Zn alloys with 0.5, 2, 4 and 8 wt.% Al at low cooling rates (under 0.00625 °C/s), and they observed a cellular microstructure in the Zn-0.5wt.%Al alloy and cellular/dendritic transition for the other alloys examined. Despite the phase diagram of Figure 2 indicates that the Zn-5wt.%Al alloy has a eutectic composition, a microstructure formed by eutectic colonies was found in this work for the 6wt.%Al composition along a range of cooling rates from 20.5 to

0.56 °C/s. Moreover, Engin et al. [65] found a eutectic microstructure, within a range of cooling rates from 2.12 to 0.045 °C/s for a Zn-5wt.%Al alloy. Spittle [66] studied Zn-(2–15)wt.%Al alloys and proposed that the coupled region is asymmetric and shifted towards the Al solid solution side of the phase diagram. That is, there is a region characterized by a range of alloys compositions and thermal parameters, in which the coupled growth occurs, and this composition range is from 5 wt.% of Al to higher values. Thus, the eutectic microstructure seems to be restricted to a narrow composition range of 5 wt.% to 6 wt.% of Al depending on the thermal parameters considered. The proposed SMSM plot could be a useful tool for condensing the information of possible microstructures taking into account the simultaneous influences of the solidification cooling rate and alloy composition. Furthermore, the range of compositions of the proposed SMSM plot, up to 12wt.%Al, may be of the interest of casting processes involving a good number of commercial Zinc–Aluminum-based alloys.
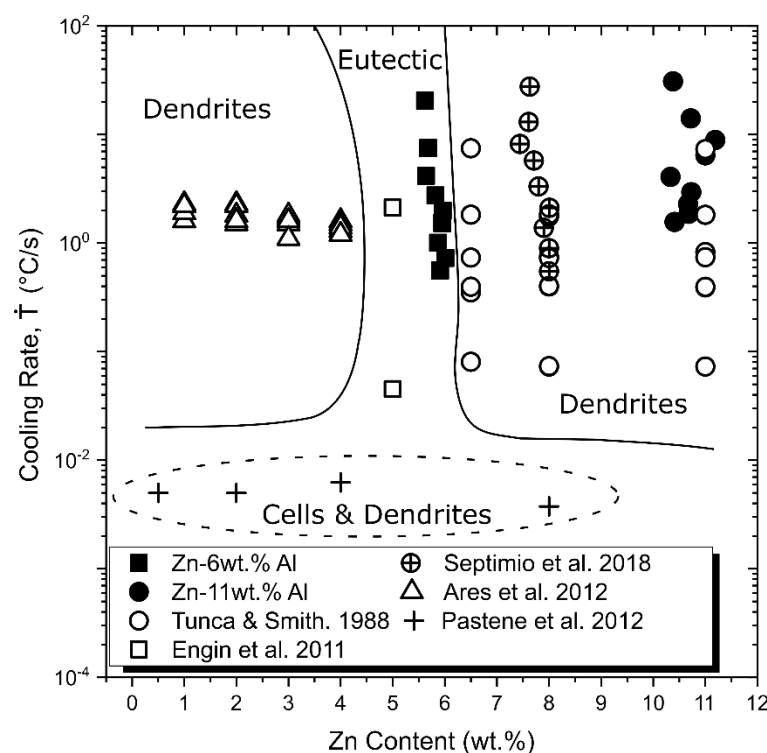

Figure 18. Coupled zone as a function of solidification cooling rate and alloy composition for Zn–Al alloys.

3.5. Vickers Microhardness (HV)

The influences of alloy Al content and length scale of the eutectic microstructure (Lamellar Eutectic Spacing) on microhardness were also investigated. The average microhardness test results of the studied alloys are presented in Figure 19. Each point on the graph represents an average of 25 measurements for each position, and the error bars are their respective standard deviations. As can be seen, the microhardness of both Zn-6wt.%Al and Zn-11wt.%Al alloys were shown not to depend on the length scale of the resulting microstructure, since HV is essentially constant. The mean Vickers microhardness of the Zn-6wt.%Al alloy was found to be 68.5 HV, while that of the Zn-11wt.%Al alloy of 71.26 HV, about 5.5% higher. Hekimoglu et al. [67] studied the effect of higher Al content (5–25%) on G-cast Zn-based alloys. They observed an increase in hardness with an increase in the alloy Al content and attributed this result to the volume fraction of the relatively hard (Al′) dendrites, combined with the solid solubility of Zn in the Al-rich phase.
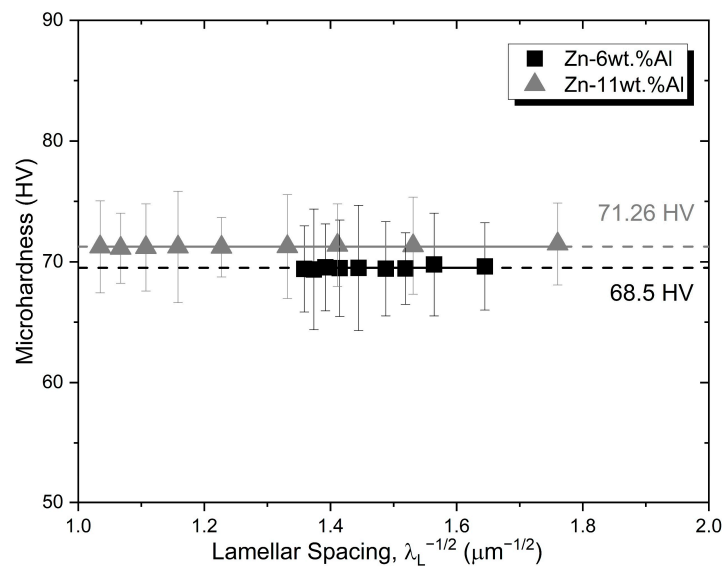
Figure 19. Vickers microhardness as a function of the lamellar eutectic spacing for the studied Zn–Al alloys.

4. Conclusions

- The microstructure of the Zn-6wt.%Al alloy was shown to be characterized by eutectic colonies, constituted by a eutectic mixture of (Zn) and (Al′) phases in the form of lamellae. Since (Al′) is a metastable phase, it undergoes a eutectoid transformation at 277 °C [(Al′)→(Al)→(Zn)]. In contrast, the Zn–11wt.% Al alloy was shown to be characterized by the presence of pro-eutectic (Al′) dendrites and interdendritic regions composed by the eutectic mixture [(Al′) + (Zn)].

- Correlations between the microstructure and the thermal parameters were established in the form of experimental growth laws relating to eutectic colony spacing (λ_{EC}); eutectic lamellae spacing (λ_L), primary dendritic arm spacing (λ_1) and secondary dendritic arm spacing (λ_2) to the thermal parameters; liquidus isotherm ($\dot{T}_L$) and eutectic isotherm ($\dot{T}_E$) cooling rates; and liquidus isotherm (V_L) and eutectic isotherm (V_E) growth rates:

Zn-6wt.%Al alloy:

$$\lambda_{EC} = 33.9 V_E^{-1/2} \text{ and } \lambda_{EC} = 79.8 \dot{T}_E^{-1/4}$$

Zn-11wt.%Al alloy:

$$\lambda_L = 0.57 V_E^{-1/2} \text{ and } \lambda_L = 0.87 \dot{T}_E^{-1/4}$$

$$\lambda_1 = 81.6 V_L^{-1.1} \text{ and } \lambda_1 = 239.8 \dot{T}_L^{-0.55}$$

$$\lambda_2 = 11 V_L^{-2/3} \text{ and } \lambda_2 = 20.3 \dot{T}_L^{-1/3}$$

where: λ_{EC}; λ_L; λ_1; λ_2 [μm]/V_E; V_L [mm/s]/$\dot{T}_E$; $\dot{T}_L$ [°C/s].

- A diagram exhibiting the coupled zone of Zn–Al alloys as a function of cooling rate ($\dot{T}$) is proposed showing different microstructural morphologies influenced by composition and thermal parameters, that is, the growth rate (V) and the temperature gradient (G), both synthesized by the cooling rate ($\dot{T}$ = G.V).

- The microhardness of both Zn-6wt.%Al and Zn-11wt.%Al alloys were shown not to depend on the length scale of the resulting microstructure, with HV being essentially constant. The mean Vickers microhardness of the Zn-11wt.%Al alloy was found to be about 5.5% higher than that of the Zn-6wt.%Al alloy.

- The approach of this research can be useful in alloys of the Zn–Al system with the addition of a third element in order to seek a better understanding of the microstructures solidified under unsteady-state solidification conditions. It is possible, in this way, to raise correlations between mechanical, wear and corrosion properties with microstructural parameters to seek the best control of the processing parameters in others to obtain the final product with specific characteristics.

Nomenclature

DS	directionally solidified
EDS	energy dispersive spectrometer
XFR	x-ray fluorescence spectrometer
XRD	x-ray diffractometry
SMSM	solidification microstructural selection map
T_L	liquidus temperature
T_E	eutectic temperature
λ_{EC}	eutectic colony spacing
λ_L	eutectic lamellae spacing
λ_1	primary dendritic arm spacing
$\lambda_2\lambda_2$	secondary dendritic arm spacing
$\dot{T}$	cooling rate
$\dot{T}_L$	cooling rate of liquidus isotherm
$\dot{T}_E$	cooling rate of eutectic isotherm
V	growth rate
V_L	growth rate of liquidus isotherm
V_L	growth rate of eutectic isotherm
G_E	gradient profiles ahead the eutectic isotherm

References

1. Zinc and Zinc Alloys. In *Metals Handbook Desk Edition*; ASM International: Almere, The Netherlands, 2018; pp. 589–597.
2. Pola, A.; Tocci, M.; Goodwin, F.E. Review of Microstructures and Properties of Zinc Alloys. *Metals* **2020**, *10*, 253. [CrossRef]
3. Türk, A.; Kurnaz, C.; Şevik, H. Comparison of the Wear Properties of Modified ZA-8 Alloys and Conventional Bearing Bronze. *Mater. Des.* **2007**, *28*, 1889–1897. [CrossRef]
4. Purcek, G.; Altan, B.S.; Miskioglu, I.; Ooi, P.H. Processing of Eutectic Zn-5% Al Alloy by Equal-Channel Angular Pressing. *J. Mater. Process. Technol.* **2004**, *148*, 279–287. [CrossRef]
5. Lachowicz, M.M.; Leśniewski, T.; Lachowicz, M.B.; Jasionowski, R. Tribological Wear of as Cast Zn-4Al Alloy Cooled at Various Rates from the Eutectoid Transformation Temperature. *Arch. Foundry Eng.* **2020**, *20*, 108–114. [CrossRef]
6. Pola, A.; Montesano, L.; Gelfi, M.; la Vecchia, G.M. Comparison of the Sliding Wear of a Novel Zn Alloy with That of Two Commercial Zn Alloys against Bearing Steel and Leaded Brass. *Wear* **2016**, *368–369*, 445–452. [CrossRef]
7. Wang, Y.Q.; Kong, G.; Che, C.S. Corrosion Behavior of Zn-Al, Zn-Mg, and Zn-Mg-Al Coatings in Simulated Concrete Pore Solution. *Corrosion* **2019**, *75*, 203–209. [CrossRef]

8. Marder, A.R. The Metallurgy of Zinc-Coated Steel. *Prog. Mater. Sci.* **2000**, *45*, 191–271. [CrossRef]

9. Li, Z.F.; He, Y.Q.; Cao, G.M.; Tang, J.J.; Zhang, X.J.; Liu, Z.Y. Effects of Al Contents on Microstructure and Properties of Hot-Dip Zn-Al Alloy Coatings on Hydrogen Reduced Hot-Rolled Steel without Acid Pickling. *J. Iron Steel Res. Int.* **2017**, *24*, 1032–1040. [CrossRef]

10. Gancarz, T.; Berent, K.; Skuza, W.; Janik, K. Soldering of Mg Joints Using Zn-Al Solders. *Metall. Mater. Trans. A Phys. Metall. Mater. Sci.* **2018**, *49*, 2684–2691. [CrossRef]

11. Rettenmayr, M.; Lambracht, P.; Kempf, B.; Tschudin, C. Zn-Al Based Alloys as Pb-Free Solders for Die Attach. *J. Electron. Mater.* **2002**, *31*, 278–285. [CrossRef]

12. Kang, N.; Na, H.S.; Kim, S.J.; Kang, C.Y. Alloy Design of Zn-Al-Cu Solder for Ultra High Temperatures. *J. Alloys Compd.* **2009**, *467*, 246–250. [CrossRef]

13. Bazhenov, V.E.; Pashkov, I.N.; Pikunov, M.V.; Cheverikin, V.V.; Anohin, A.A. Interaction of Zn and Zn-4Al, Zn-15Al (Wt-%) Solder Alloys with Aluminium. *Mater. Sci. Technol.* **2016**, *32*, 752–759. [CrossRef]

14. Santos, G.A.; de Moura, C.; Oso, W.R. Design of Mechanical Properties of a Zn27Al Alloy Based on Microstructure Dendritic Array Spacing. *Mater. Des.* **2007**, *28*, 2425–2430. [CrossRef]

15. Osório, W.R.; Garcia, A. Modeling Dendritic Structure and Mechanical Properties of Zn-Al Alloys as a Function of Solidification Conditions. *Mater. Sci. Eng. A* **2002**, *325*, 103–111. [CrossRef]

16. Bertelli, F.; Brito, C.; Ferreira, I.L.; Reinhart, G.; Nguyen-Thi, H.; Mangelinck-Noël, N.; Cheung, N.; Garcia, A. Cooling Thermal Parameters, Microstructure, Segregation and Hardness in Directionally Solidified Al-Sn-(Si;Cu) Alloys. *Mater. Des.* **2015**, *72*, 31–42. [CrossRef]

17. Vida, T.A.; Brito, C.; Lima, T.S.; Spinelli, J.E.; Cheung, N.; Garcia, A. Near-Eutectic Zn-Mg Alloys: Interrelations of Solidification Thermal Parameters, Microstructure Length Scale and Tensile/Corrosion Properties. *Curr. Appl. Phys.* **2019**, *19*, 582–598. [CrossRef]

18. Barnhurst, R.J. Zinc and Zinc Alloys. In *Properties and Selection: Nonferrous Alloys and Special-Purpose Materials*; ASM International: Almere, The Netherlands, 1990.

19. Apelian, D.; Paliwal, M.; Herrschaft, D.C. Casting with Zinc Alloys. *J. Met.* **1981**, 12–20. [CrossRef]

20. Septimio, R.S.; Costa, T.A.; Silva, C.A.P.; Vida, T.A.; de Damborenea, J.; Garcia, A.; Cheung, N. Correlation between Unsteady-State Solidification Thermal Parameters and Microstructural Growth of Zn–8 Mass% Al and Zn–8 Mass% Al–XBi Tribological Alloys. *J. Therm. Anal. Calorim.* **2020**, *139*, 1741–1761. [CrossRef]

21. Murray, J.L. The Al-Zn (Aluminum-Zinc) System. *Bull. Alloy Phase Diagr.* **1983**, *4*, 55–73. [CrossRef]

22. Abou El-Khair, M.T.; Daoud, A.; Ismail, A. Effect of Different Al Contents on the Microstructure, Tensile and Wear Properties of Zn-Based Alloy. *Mater. Lett.* **2004**, *58*, 1754–1760. [CrossRef]

23. Bansod, A.; Patil, A.P.; Deshmukh, B. Microstructural and Corrosion Behavior of Different Aluminum Content on Zinc. In Proceedings of the CORCON 2018, Jaipur, India, 1 December 2018; p. 0MC15.

24. Osório, W.R.; Santos, C.A.; Quaresma, J.M.V.; Garcia, A. Mechanical Properties as a Function of Thermal Parameters and Microstructure of Zn-Al Castings. *J. Mater. Process. Technol.* **2003**, *143–144*, 703–709. [CrossRef]

25. Porot, P.A.; Spittle, J.A. Structural Variation in Near-Eutectic Zinc-Aluminum Alloys. *Metallography* **1987**, *197*, 181–197. [CrossRef]

26. Kurz, W.; Fisher, D.J. Solidification Microstructure- Processing Maps: Theoryand Application. *Adv. Eng. Mater.* **2001**, *3*, 443–452. [CrossRef]

27. Silva, C.A.P.; Kakitani, R.; Canté, M.V.; Brito, C.; Garcia, A.; Spinelli, J.E.; Cheung, N. Microstructure, Phase Morphology, Eutectic Coupled Zone and Hardness of Al–Co Alloys. *Mater. Charact.* **2020**, *169*, 110617. [CrossRef]

28. Kakitani, R.; Pinto da Silva, C.A.; Silva, B.; Garcia, A.; Cheung, N.; Spinelli, J.E. Local Solidification Thermal Parameters Affecting the Eutectic Extent in Sn-Cu and Sn-Bi Solder Alloys. *Solder. Surf. Mt. Technol.* **2022**, *34*, 24–30. [CrossRef]

29. Rai, P.K.; Rout, D.; Satish Kumar, D.; Sharma, S.; Balachandran, G. Effect of Magnesium on Corrosion Behavior of Hot-Dip Zn-Al-Mg Coating. *J. Mater. Eng. Perform.* **2021**, *30*, 4138–4147. [CrossRef]

30. Xie, Y.; Du, A.; Zhao, X.; Ma, R.; Fan, Y.; Cao, X. Effect of Mg on Fe–Al Interface Structure of Hot–Dip Galvanized Zn–Al–Mg Alloy Coatings. *Surf. Coat. Technol.* **2018**, *337*, 313–320. [CrossRef]

31. Yu, K.C.; Li, J.; Liu, X.; Li, J.G.; Xue, X.H. Microstructure of Hot-Dip Galvanized Zn-Al-Mg Alloy Coating. *J. Shanghai Jiaotong Univ. (Sci.)* **2012**, *17*, 663–667. [CrossRef]

32. Prosek, T.; Hagström, J.; Persson, D.; Fuertes, N.; Lindberg, F.; Chocholatý, O.; Taxén, C.; Šerák, J.; Thierry, D. Effect of the Microstructure of Zn-Al and Zn-Al-Mg Model Alloys on Corrosion Stability. *Corros. Sci.* **2016**, *110*, 71–81. [CrossRef]

33. TCS Solder Alloy Solutions Database (TCSLD3), Thermocalc. 2020. Available online: https://www.engineering-eye.com/THERMOCALC/details/db/pdf/thermo-calc/06/tcsld3-2_extended_info.pdf (accessed on 22 June 2022).

34. Gündüz, M.; Çadirli, E. Directional Solidification of Aluminium-Copper Alloys. *Mater. Sci. Eng. A* **2002**, *327*, 167–185. [CrossRef]

35. Spinelli, J.E.; Silva, B.L.; Cheung, N.; Garcia, A. The Use of a Directional Solidification Technique to Investigate the Interrelationship of Thermal Parameters, Microstructure and Microhardness of Bi-Ag Solder Alloys. *Mater. Charact.* **2014**, *96*, 115–125. [CrossRef]

36. Çadirli, E.; Marasli, N.; Bayender, B.; Gündüz, M. Dependency of the Microstructure Parameters on the Solidification Parameters for Camphene. *Mater. Res. Bull.* **2000**, *35*, 985–995. [CrossRef]

37. Kaya, H.; Çadirli, E.; Ülgen, A. Investigation of the Effect of Composition on Microhardness and Determination of Thermo-Physical Properties in the Zn-Cu Alloys. *Mater. Des.* **2011**, *32*, 900–906. [CrossRef]

38. Vida, T.A.; Soares, T.; Septimio, R.S.; Brito, C.C.; Cheung, N.; Garcia, A. Effects of Macrosegregation and Microstructure on the Corrosion Resistance and Hardness of a Directionally Solidified Zn-5.0wt.%Mg Alloy. *Mater. Res.* **2019**, *22*, 1–13. [CrossRef]

39. Dias, M.; Brito, C.; Bertelli, F.; Rocha, O.L.; Garcia, A. Interconnection of Thermal Parameters, Microstructure, Macrosegregation and Microhardness of Unidirectionally Solidified Zn-Rich Zn-Ag Peritectic Alloys. *Mater. Des.* **2014**, *63*, 848–855. [CrossRef]

40. Li, Z.; He, Y.; Cao, G.; Tang, J.; Zhang, X.; Liu, Z. Modifications on Solidification Thermal Parameters, Microstructure and Hardness Induced by Cu Additions to a Hypereutectic Zn–8Al Alloy. *J. Iron Steel Res.* **2017**, *174*, 1032–1040. [CrossRef]

41. Silva, B.L.; Cheung, N.; Garcia, A.; Spinelli, J.E. Evaluation of Solder/Substrate Thermal Conductance and Wetting Angle of Sn-0.7 Wt%Cu-(0-0.1 Wt%Ni) Solder Alloys. *Mater. Lett.* **2015**, *142*, 163–167. [CrossRef]

42. MatWeb. Zinc, Zn. Available online: https://www.matweb.com/search/DataSheet.aspx?MatGUID=8909140a76074049809ad74d536ed606&ckck=1 (accessed on 16 May 2022).

43. McAlister, A.; Orr, C. Thermal Conductivities of Aluminum and Zinc Powder Suspensions. *J. Chem. Eng. Data* **1964**, *9*, 71–74. [CrossRef]

44. Kurz, W.; Fisher, D.J. *Fundamentals of Solidification*, 3rd ed.; Trans Tech Publications: Stafa-Zurich, Switzerland, 1990.

45. Łent, M.T. Coupled and Competitive Eutectic Growth. *Arch. Foundry Eng.* **2011**, *11*, 237–240.

46. Neikov, O.D. Production of Aluminum Alloy Powders. In *Handbook of Non-Ferrous Metal Powders*; S. Banerjee, P.M., Ed.; Elsevier Ltd.: Amsterdam, The Netherlands, 2007; pp. 481–531. ISBN 9780081005439.

47. Chapter 3 Solidification, Vitrification, Crystallization and Formation of Quasicrystalline and Nanocrystalline Structures. In *Phase Transformations: Examples from Titanium and Zirconium Alloys*; Banerjee, S., Mukhopadhyay, P., Eds.; Elsevier: Amsterdam, The Netherlands, 2007; Volume 12, pp. 125–255. ISBN 9780080421452.

48. Ji, Y.; Heo, T.W.; Zhang, F.; Chen, L.Q. Theoretical Assessment on the Phase Transformation Kinetic Pathways of Multi-Component Ti Alloys: Application to Ti-6Al-4V. *J. Phase Equilibria Diffus.* **2016**, *37*, 53–64. [CrossRef]

49. Garcia, A. *Solidificação: Fundamentos E Aplicações*; Editora Unicamp: Campinas, Brazil, 2007.

50. Gill, S.C.; Zimmermann, M.; Kurz, W. Laser Resolidification of the A1-A12Cu Eutectic: The Coupled Zone. *Acta Metall. Mater.* **1992**, *40*, 2895–2906. [CrossRef]

51. Abboud, J.; Mazumder, J. Developing of Nano Sized Fibrous Eutectic Silicon in Hypereutectic Al–Si Alloy by Laser Remelting. *Sci. Rep.* **2020**, *10*, 12090. [CrossRef] [PubMed]

52. Kang, J.L.; Li, J.F. The Growth Pattern of Co_3Sn_2 in Directional Solidification of Co-Sn Hypereutectic Alloy Melts. *Metall. Mater. Trans. A Phys. Metall. Mater. Sci.* **2020**, *51*, 6346–6354. [CrossRef]

53. Jackson, K.A.; Hunt, J.D. Lamellar and Rod Eutectic Growth. *Dyn. Curved Front.* **1988**, *236*, 363–376. [CrossRef]

54. Garcia, A.; Clyne, T.W.; Prates, M. Mathematical Model for the Unidirectional Solidification of Metals: II. Massive Molds. *Metall. Trans. B* **1979**, *10*, 85–92. [CrossRef]

55. Kakitani, R.; Reyes, R.V.; Garcia, A.; Spinelli, J.E.; Cheung, N. Relationship between Spacing of Eutectic Colonies and Tensile Properties of Transient Directionally Solidified Al-Ni Eutectic Alloy. *J. Alloys Compd.* **2018**, *733*, 59–68. [CrossRef]

56. Spinelli, J.E.; Silva, B.L.; Garcia, A. Microstructure, Phases Morphologies and Hardness of a Bi-Ag Eutectic Alloy for High Temperature Soldering Applications. *Mater. Des.* **2014**, *58*, 482–490. [CrossRef]

57. Haghdadi, N.; Phillion, A.B.; Maijer, D.M. Microstructure Characterization and Thermal Analysis of Aluminum Alloy B206 during Solidification. *Metall. Mater. Trans. A Phys. Metall. Mater. Sci.* **2015**, *46*, 2073–2081. [CrossRef]

58. Xavier, M.G.C.; Souza, T.M.G.; Cheung, N.; Garcia, A.; Spinelli, J.E. Effects of Cobalt and Solidification Cooling Rate on Intermetallic Phases and Tensile Properties of a -Cu, -Zn, -Fe Containing Al-Si Alloy. *Int. J. Adv. Manuf. Technol.* **2020**, *107*, 717–730. [CrossRef]

59. Kakitani, R.; Cruz, C.B.; Lima, T.S.; Brito, C.; Garcia, A.; Cheung, N. Transient Directional Solidification of a Eutectic Al–Si–Ni Alloy: Macrostructure, Microstructure, Dendritic Growth and Hardness. *Materialia* **2019**, *7*, 100358. [CrossRef]

60. Xavier, M.G.C.; Cruz, C.B.; Kakitani, R.; Silva, B.L.; Garcia, A.; Cheung, N.; Spinelli, J.E. Directional Solidification of a Sn-0.2Ni Solder Alloy in Water-Cooled Copper and Steel Molds: Related Effects on the Matrix Micromorphology, Nature of Intermetallics and Tensile Properties. *J. Alloys Compd.* **2017**, *723*, 1039–1052. [CrossRef]

61. Silva, B.L.; Cheung, N.; Garcia, A.; Spinelli, J.E. Sn-0.7 Wt%Cu-(XNi) Alloys: Microstructure-Mechanical Properties Correlations with Solder/Substrate Interfacial Heat Transfer Coefficient. *J. Alloys Compd.* **2015**, *632*, 274–285. [CrossRef]

62. Tunca, N.; Smith, R.W. Variation of Dendrite Arm Spacing in AI-Rich Zn-AI off-Eutectic Alloys. *J. Mater. Sci.* **1988**, *23*, 111–120. [CrossRef]

63. Ares, A.E.; Gassa, L.M.; Schvezov, C.E.; Rosenberger, M.R. Corrosion and Wear Resistance of Hypoeutectic Zn-Al Alloys as a Function of Structural Features. *Mater. Chem. Phys.* **2012**, *136*, 394–414. [CrossRef]

64. Pastene, M.P.; Fornaro, O.; Medina, H.O. Study of Directional Solidification of Zn-Al Alloys. *Procedia Mater. Sci.* **2012**, *1*, 87–94. [CrossRef]

65. Engin, S.; Böyük, U.; Kaya, H.; Maraşlı, N. Directional Solidification and Physical Properties Measurements of the Zinc-Aluminum Eutectic Alloy. *Int. J. Miner. Metall. Mater.* **2011**, *18*, 659–664. [CrossRef]

66. Spittle, J.A. Endogenous-Exogenous Freezing Characteristics of Pure and Impure as-Cast Zn-AI Alloys. *Met. Sci.* **1977**, *11*, 578–585. [CrossRef]

67. Hekimoğlu, A.P.; Savaşkan, T. Structure and Mechanical Properties of Zn-(5–25) Al Alloys. *Int. J. Mater. Res.* **2014**, *105*, 1084–1089. [CrossRef]